Originals Computational Mechanics 20 (1997) 495–506 © Springer-Verlag 1997

Fast multipole method as an efficient solver for 2D elastic wave surface integral equations

Y. H. Chen, W. C. Chew, S. Zeroug

Abstract The fast multipole method (FMM) is very efficient in solving integral equations. This paper applies the method to solve large solid-solid boundary integral equations for elastic waves in two dimensions. The scattering problem is first formulated with the boundary element method. FMM is then introduced to expedite the solution process. By using the FMM technique, the number of floating-point operations of the matrix-vector multiplication in a standard conjugate gradient algorithm is reduced from $O(N^2)$ to $O(N^{1.5})$, where N is the number of unknowns. The matrix-filling time and the memory requirement are also of the order $N^{1.5}$. The computational complexity of the algorithm is further reduced to $O(N^{4/3})$ by using a ray propagation technique. Numerical results are given to show the accuracy and efficiency of FMM compared to the boundary element method with dense matrix.

1 Introduction

The elastic wave (beam) scattering from a solid-solid interface is of great interest to a wide range of disciplines such as geophysical exploration, non-destructive evaluation, mechanical design, etc. Since elastic waves are characterized by both displacement fields and stress fields which propagate and cover large spatial domains (in terms of the operating wavelength), a large number of unknowns are often involved in the numerical modeling. For large problems, iterative methods such as conjugate gradient (CG) methods are preferred over direct methods. The major computational cost of an iterative method lies in the matrix-vector multiplications. In a standard dense matrix boundary element method (Rizzo 1967; Cole et al. 1978; Brebbia et al. 1984; Manolis and Beskos 1988; Nihei et al. 1995), or the method of moment (MoM) in the electromagnetic community (Harrington 1968), the number of floating-point operations of a matrix-vector multiplication is $O(N^2)$, where N is the number of unknowns involved. The memory requirement is also of $O(N^2)$. Iterative methods are superior to direct methods when the number of iterations required for convergence is small, and when the number of right-hand sides is small. However, when N is big (unfortunately this is often the case), the dense matrix methods become prohibitively slow and impractical.

In order to solve large problems, researchers have developed various techniques to reduce computational complexities. Most of the techniques, however, are approximate methods and have limited applications. The well-known Kirchhoff approximation and the small perturbation method (Tsang et al. 1985) are only applicable for short wavelength and small rough surface scattering respectively. Methods based on fast Fourier transforms are inefficient because of their strict uniform grid requirement. The wavelet technique has received much attention in recent years, but studies (Wagner and Chew 1995) show that, while reducing solution time by a constant factor, the technique does not reduce its computational complexity.

The fast multipole method (FMM) is designed to speed up the matrix-vector multiplications in an iterative method. The method was first introduced by Rokhlin (1990) to solve acoustic wave scattering problems. Engheta et al. (1992) applied the method to electromagnetic scattering computation of the E_z-polarized case. Lu and Chew (1993) extended the algorithm to the H_z-polarized case and applied it to calculate the scattering solution of dielectric-coated conducting cylinders. The application of the method to three dimensional electromagnetic wave scattering has been studied by Coifman et al. (1993), and Song and Chew (1994).

The idea behind FMM is to first divide the subscatterers into groups. Then, the addition theorem of the Bessel functions is used to translate the scattered fields of different scattering centers within a group into a single center (the group center). Namely, we represent the scattered fields of a group of scatterers as waves emanating from its group center by using the addition theorem. Next, the interactions among these groups are calculated. That is,

Communicated by S. N. Atluri, 24 April 1997

Y. H. Chen, W. C. Chew
Center for Computational Electromagnetics,
Department of Electrical and Computer Engineering,
University of Illinois, Urbana, IL 61801, USA

S. Zeroug
Geoacoustic Department, Schlumberger-Doll Research,
Old Quarry Road, Ridgefield, CT 06877, USA

Correspondence to: Y. H. Chen

This work was supported by the Air Force Office of Scientific Research under Grant No. F49620-96-1-0025, the National Science Foundation under Grant No. NSF ECS93-02145, the Office of Naval Research under Grant No. N00014-95-1-0872, and a gift from Schlumberger-Doll Research. The first author would like to thank Jiming Song and Chung Chang for some useful discussions.

the scattered fields of all other groups are calculated at each group around its center. Finally, the addition theorem is again used to translate the scattered fields around the group center to its group members (the subscatterers in the group). As stated in the paper by Lu and Chew (1993), the above procedure will not reduce the computational complexity because the group center requires a higher-order multipole. The reduction in the number of scattering centers is at the expense of increasing the order of the multipoles. However, significant computational savings can be achieved by diagonalizing the translation matrix that accounts for interactions among the groups using plane-wave bases and by appropriately selecting the size of groups. The technique reduces the matrix-vector multiplication from $O(N^2)$ for dense matrix methods to $O(N^{1.5})$ in an iterative method. It can be easily extended to an $O(N^{4/3})$ algorithm by using a ray propagation technique (Wagner and Chew 1994; Coifman et al. 1994).

In this paper, we apply the fast multipole method and the ray propagation fast multipole technique to the boundary element methods (BEM) for elastic wave modeling. We discuss how the new techniques are used to solve two-dimensional solid-solid surface scattering problems where the solids are assumed to be bonded at the interfaces. In what follows, we present the formulation of the surface integral equations for elastic-wave fields. The integral equations are converted into a linear equation set based on the pulse basis-point matching scheme. The fast multipole method and the ray propagation technique are then introduced to speed up the solution process. Finally, we apply the technique to solve planar and rough solid-solid surface scattering problems. The numerical results are validated by an analytical approach and a dense-matrix BEM code.

2 Surface integral equations

Consider two elastic media separated by an arbitrary surface S_0 as shown in Figure 1. The upper region is denoted as Ω_0 and is occupied by an isotropic homogeneous medium characterized by mass density ρ_0 and Lamé constants λ_0 and μ_0. The lower region is denoted as Ω_1 and is occupied by another isotropic homogeneous medium characterized by mass density ρ_1 and Lamé constants λ_1 and μ_1. The unit normal vector of the surface is defined by $\hat{\mathbf{n}}(\mathbf{r})$, where $\mathbf{r} = (x, z)$. In the following formulation, we use uppercase boldface letters for vector fields, and reserve lowercase boldface letters for column vectors and spatial coordinates. Matrices and second rank tensors are represented by uppercase boldface letters with a bar on the top. Two bars are placed on an uppercase boldface letter to represent a third rank tensor. Given a function $g(x, z)$, the notations for differentiation are defined as followings,

$$\partial_x g = \frac{\partial g}{\partial x}, \quad \partial^2_{xx} g = \frac{\partial^2 g}{\partial x^2}, \quad \partial^3_{xxz} g = \frac{\partial^3 g}{\partial x^2 \partial z} \ .$$

Suppose we have a force distribution $\mathbf{F}(\mathbf{r}')e^{-i\omega t}$ inside the closed surface, where ω is the angular frequency. The force will generate stress and displacement fields in the media. The displacement vector $\mathbf{U}(\mathbf{r})$ and the stress tensor $\bar{\mathbf{T}}(\mathbf{r})$ satisfy the following surface integral equations (SIE) for a bonded interface S_0 (Varadan et al. 1991; Nihei et al. 1995),

$$\frac{1}{2}\mathbf{U}(\mathbf{r}) + \int_{S_0} \left\{ \mathbf{U}(\mathbf{r}') \cdot \left[\hat{\mathbf{n}}' \cdot \overline{\overline{\mathbf{\Sigma}}}^{0}(\mathbf{r}, \mathbf{r}') \right] - [\hat{\mathbf{n}}' \cdot \bar{\mathbf{T}}(\mathbf{r}')] \cdot \bar{\mathbf{G}}^0(\mathbf{r}, \mathbf{r}') \right\} dl' = \mathbf{U}^{\text{inc}}(\mathbf{r}) \ , \quad (1)$$

$$-\frac{1}{2}\mathbf{U}(\mathbf{r}) + \int_{S_0} \left\{ \mathbf{U}(\mathbf{r}') \cdot \left[\hat{\mathbf{n}}' \cdot \overline{\overline{\mathbf{\Sigma}}}^{1}(\mathbf{r}, \mathbf{r}') \right] - [\hat{\mathbf{n}}' \cdot \bar{\mathbf{T}}(\mathbf{r}')] \cdot \bar{\mathbf{G}}^1(\mathbf{r}, \mathbf{r}') \right\} dl' = 0 \ , \quad (2)$$

where both $\mathbf{r}, \mathbf{r}' \in S_0$ and $\hat{\mathbf{n}}' = \hat{\mathbf{n}}(\mathbf{r}')$. The incident field $\mathbf{U}^{\text{inc}}(\mathbf{r})$ is given as

$$\mathbf{U}^{\text{inc}}(\mathbf{r}) = \int_{\Omega_0} \mathbf{F}(\mathbf{r}') \cdot \bar{\mathbf{G}}^0(\mathbf{r}, \mathbf{r}') d\mathbf{r}' \ , \quad (3)$$

where $\bar{\mathbf{G}}^0(\mathbf{r}, \mathbf{r}')$ is the Green's displacement tensor in Ω^0. It satisfies the following vector wave equation,

$$\left[(\lambda + \mu)\nabla\nabla \cdot + \mu\nabla^2\right]\bar{\mathbf{G}}(\mathbf{r}, \mathbf{r}') + \rho\omega^2\bar{\mathbf{G}}(\mathbf{r}, \mathbf{r}') = -\delta(\mathbf{r} - \mathbf{r}')\bar{\mathbf{I}} \ , \quad (4)$$

where $\mathbf{r}$ and $\mathbf{r}'$ are the observation point and the source point respectively and $\bar{\mathbf{I}}$ is the identity tensor. For an infinitely extended region, the solution to the above vector wave equation is given by Morse and Feshbach (1953):

$$\bar{\mathbf{G}}(\mathbf{r}, \mathbf{r}') = \frac{1}{\omega^2\rho}\left[k_s^2 g_s \bar{\mathbf{I}} + \nabla(g_p - g_s)\nabla'\right] \ , \quad (5)$$

where g_p and g_s are the whole space scalar Green's functions for the compressional and the shear waves respectively. for two dimensional problems, $g_p = \frac{i}{4}H_0^{(1)}(k_p|\mathbf{r} - \mathbf{r}'|)$, and $g_s = \frac{i}{4}H_0^{(1)}(k_s|\mathbf{r} - \mathbf{r}'|)$ with $k_p = \omega/v_p$ and $k_s = \omega/v_s$, where v_p and v_s are the compressional and shear wavespeeds. Using the constitutive relationship, the third rank Green's stress tensor, Σ, can be readily written as

$$\overline{\overline{\mathbf{\Sigma}}}(\mathbf{r}, \mathbf{r}') = \lambda\bar{\mathbf{I}}\nabla \cdot \bar{\mathbf{G}} + \mu(\nabla\bar{\mathbf{G}} + \bar{\mathbf{G}}\nabla) \ . \quad (6)$$

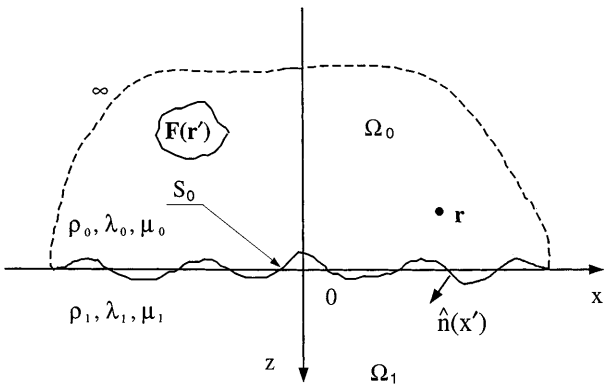

Fig. 1. The surface scattering model for the boundary integral equations

By letting $\hat{\mathbf{n}}' \cdot \bar{\mathbf{T}}(\mathbf{r}') = T_x\hat{\mathbf{x}} + T_z\hat{\mathbf{z}}$, where $T_x = n'_x T_{xx} + n'_z T_{zx}$ and $T_z = n'_x T_{xz} + n'_z T_{zz}$, and substituting the expression into the vector surface integral Eqs. 1 and 2, we obtain four scalar SIEs:

$$\frac{1}{2}U_x(\mathbf{r}) + \int_{S_0}\Big(U_x n'_x\Sigma^0_{xxx} + U_x n'_z\Sigma^0_{xxx} + U_z n'_x\Sigma^0_{xzx} + U_z n'_z\Sigma^0_{zzx} - T_x G^0_{xx} - T_z G^0_{zx}\Big)\mathrm{d}l' = U^{\mathrm{inc}}_x(\mathbf{r}) \ , \quad (7)$$

$$\frac{1}{2}U_z(\mathbf{r}) + \int_{S_0}\Big(U_z n'_z\Sigma^0_{zzz} + U_z n'_x\Sigma^0_{xzz} + U_x n'_z\Sigma^0_{zxz} + U_x n'_x\Sigma^0_{xxz} - T_x G^0_{xz} - T_z G^0_{zz}\Big)\mathrm{d}l' = U^{\mathrm{inc}}_z(\mathbf{r}) \ , \quad (8)$$

$$-\frac{1}{2}U_x(\mathbf{r}) + \int_{S_0}\Big(U_x n'_x\Sigma^1_{xxx} + U_x n'_z\Sigma^1_{zxx} + U_z n'_x\Sigma^1_{xzx} + U_z n'_z\Sigma^1_{zzx} - T_x G^1_{xx} - T_z G^1_{zx}\Big)\mathrm{d}l' = 0 \ , \quad (9)$$

and

$$-\frac{1}{2}U_z(\mathbf{r}) + \int_{S_0}\Big(U_z n'_z\Sigma^1_{zzz} + U_z n'_x\Sigma^1_{xzz} + U_x n'_z\Sigma^1_{zxz} + U_x n'_x\Sigma^1_{xxz} - T_x G^1_{xz} - T_z G^1_{zz}\Big)\mathrm{d}l' = 0 \ . \quad (10)$$

Thus, we have four unknowns $U_x = U_x(\mathbf{r}')$, $U_z = U_z(\mathbf{r}')$, $T_x = T_x(\mathbf{r}')$, and $T_z = T_z(\mathbf{r}')$ and four scalar equations. The boundary element method can be used to solve the surface unknowns. Once we know the displacement fields $\mathbf{U}(\mathbf{r}')$ and the tractions $\hat{\mathbf{n}}' \cdot \bar{\mathbf{T}}(\mathbf{r}')$ on the interface, the following equations can be used to calculate the displacement fields everywhere in Ω_0 and Ω_1 respectively,

$$\mathbf{U}(\mathbf{r}) = \mathbf{U}^{inc}(\mathbf{r}) + \int_{S_0}\left\{[\hat{\mathbf{n}}' \cdot \bar{\mathbf{T}}(\mathbf{r}')] \cdot \bar{\mathbf{G}}^0(\mathbf{r},\mathbf{r}') - \mathbf{U}(\mathbf{r}') \cdot \left[\hat{\mathbf{n}}' \cdot \overset{=0}{\Sigma}(\mathbf{r},\mathbf{r}')\right]\right\}\mathrm{d}l' \ , \quad (11)$$

$$\mathbf{U}(\mathbf{r}) = \int_{S_0}\left\{\mathbf{U}(\mathbf{r}') \cdot \left[\hat{\mathbf{n}}' \cdot \overset{=1}{\Sigma}(\mathbf{r},\mathbf{r}')\right] - [\hat{\mathbf{n}}' \cdot \bar{\mathbf{T}}(\mathbf{r}')] \cdot \bar{\mathbf{G}}^1(\mathbf{r},\mathbf{r}')\right\}\mathrm{d}l' \ . \quad (12)$$

The constitutive relation equation can be used to determine the stress tensor from the displacement fields.

3 Boundary element method formulation

In this section, we discuss how the SIEs (7)–(10) can be converted into a set of linear equations which can be solved by a computer. To solve the surface unknowns $U_x(\mathbf{r}')$, $U_z(\mathbf{r}')$, $T_x(\mathbf{r}')$, and $T_z(\mathbf{r}')$ with the boundary element method, we first expand the surface field components in terms of basis functions, and then test the equation with weighting functions. In general, either full-domain or subdomain basis functions can be used to expand the unknown fields as long as the set of basis functions is complete. However, it is often difficult to find such a set of full-domain basis functions, and for different problems, the full-domain basis functions are usually different. On the contrary, the subdomain basis is more versatile and is widely used for various problems. Thus, we choose the subdomain basis for out problem. Specifically, in the following formulation of the moment method, we use the pulse basis functions to expand the surface unknowns and the Dirac delta functions to test the SIEs for ease of implementation. So, we discretize the surface into N segments with approximately equal length and expand the surface field unknowns with the pulse basis function, i.e.,

$$U_x(\mathbf{r}') = \sum_{n=1}^{N} U^x_n P_n(\mathbf{r}'), \quad U_z(\mathbf{r}') = \sum_{n=1}^{N} U^z_n P_n(\mathbf{r}') \ ,$$

and

$$T_x(\mathbf{r}') = \sum_{n=1}^{N} T^x_n P_n(\mathbf{r}'), \quad T_z(\mathbf{r}') = \sum_{n=1}^{N} T^z_n P_n(\mathbf{r}') \ ,$$

where U^x_n, U^z_n, T^x_n and T^z_n with $n = 1, \ldots, N$ are the unknown coefficients to be determined. The pulse basis function $P_n(\mathbf{r})(n = 1, 2, \ldots, N)$ has a constant unity value on the nth segment and vanishes outside its two end points $\mathbf{r}_n$ and $\mathbf{r}_{n+1}$.

To convert Eq. (7) into linear algebraic equations, we substitute the expression of U_x, U_z, T_x, and T_z into the equation, multiply both sides with $\delta(\mathbf{r} - \mathbf{r}_m)$, and integrate with respect to x over the surface. We obtain the following linear algebraic equations:

$$\sum_{n=1}^{N}\left(A^1_{mn}U^x_n + B^1_{mn}U^z_n + C^1_{mn}T^x_n + D^1_{mn}T^z_n\right) = b^1_m, \quad m = 1, 2, \ldots, N \ , \quad (13)$$

where $b^1_m = U^{\mathrm{inc}}_x(\mathbf{r}_m)$ and A^1_{mn}, B^1_{mn}, C^1_{mn}, and D^1_{mn} are constant coefficients given by

$$A^1_{mn} = \frac{1}{2}\delta_{mn} + \int_{S_0} P_n(\mathbf{r}')\Big(n'_x\Sigma^0_{xxx} + n'_z\Sigma^0_{zxx} + n'_x\Sigma^0_{xzx}\Big)\mathrm{d}l' \ , \quad (14)$$

$$B^1_{mn} = \int_{S_0} P_n(\mathbf{r}')\left(n'_x\Sigma^0_{xzx} + n'_z\Sigma^0_{zzx}\right)\mathrm{d}l' \ , \quad (15)$$

$$C^1_{mn} = -\frac{1}{\omega^2\rho}\int_{S_0} P_n(\mathbf{r}')\left[k_s^2 g^0_s + \partial^2_{x'x'}\left(g^0_s - g^0_p\right)\right]\mathrm{d}l' \ , \quad (16)$$

and

$$D^1_{mn} = -\frac{1}{\omega^2\rho}\int_{S_0} P_n(\mathbf{r}')\partial^2_{z'x'}\left(g^0_s - g^0_p\right)\mathrm{d}l' \ , \quad (17)$$

where $R_m = |\mathbf{r}' - \mathbf{r}_m|$. Notice that $\Sigma_{ijk}, \{i, j, k\} = \{x, y, z\}$, are given by Eq. (6). We did not substitute them into the expressions for A^1_{mn} and B^1_{mn} in favor of conciseness. The normal direction of the nth segment is defined by $\hat{\mathbf{n}}' = n'_x\hat{\mathbf{x}} + n'_z\hat{\mathbf{z}}$, where n'_x and n'_z are given as

$$n'_x = -\frac{z_{n+1}-z_n}{\sqrt{(x_{n+1}-x_n)^2+(z_{n+1}-z_n)^2}},$$
$$n'_z = -\frac{x_{n+1}-x_n}{\sqrt{(x_{n+1}-x_n)^2+(z_{n+1}-z_n)^2}} \quad . \tag{18}$$

The matrix elements are calculated directly from the above formulae for non-diagonal terms ($m \neq n$). For diagonal terms, the Green's functions are singular when $|\mathbf{r}' - \mathbf{r}_m|$ approaches zero. However, the integrands for both A^1_{mm} and B^1_{mm} are odd functions for the central point (x_m, z_m). The Cauchy principal integrals thus vanish for the self-terms. Therefore, we have

$$A^1_{mm} = 0.5, \quad B^1_{mm} = 0, \quad m = 1, 2, \ldots N \quad . \tag{19}$$

The diagonal elements C^1_{mm} and D^1_{mm} need to be evaluated very carefully, because the Green's function contains an integrable singularity at $\mathbf{r} = \mathbf{r}'$. The procedure used to treat these singularities is to substract the singular term from the integrand to make it regular so that standard numerical integration methods can be applied. The singular term substracted here is the small argument approximation of the integrand. The contribution of the singular term to the diagonal element is calculated analytically.

Similarly, The linear system corresponding to the surface integral Eq. (8) can be written as

$$\sum_{n=1}^{N}\left(A^2_{mn}U^x_n + B^2_{mn}U^z_n + C^2_{mn}T^x_n + D^2_{mn}T^z_n\right) = b^2_m,$$
$$m = 1, 2, \ldots, N \quad , \tag{20}$$

where $b^2_m = U^{\text{inc}}_z(\mathbf{r}_m)$. The constant coefficients A^2_{mn}, B^2_{mn}, C^2_{mn}, and D^2_{mn} are defined by

$$A^2_{mn} = \int_{S_0} P_n(\mathbf{r}')\left(n'_z\Sigma^0_{zxz} + n'_x\Sigma^0_{xxz}\right)\mathrm{d}l' \quad , \tag{21}$$

$$B^2_{mn} = \frac{1}{2}\delta_{mn} + \int_{S_0} P_n(\mathbf{r}')\left(n'_z\Sigma^0_{zzz} + n'_x\Sigma_{xzz}\right)\mathrm{d}l' \quad , \tag{22}$$

$$C^2_{mn} = -\frac{1}{\omega^2\rho}\int_{S_0} P_n(\mathbf{r}')\partial^2_{x'z'}\left(g^0_s - g^0_p\right)\mathrm{d}l' \quad , \tag{23}$$

and

$$D^2_{mn} = -\frac{1}{\omega^2\rho}\int_{S_0} P_n(\mathbf{r}')\left[k^2_s g^0_s + \partial^2_{z'z'}\left(g^0_s - g^0_p\right)\right]\mathrm{d}l' \quad . \tag{24}$$

Again, the above expression can be readily used to calculate off-diagonal elements. The diagonal elements are evaluated by using the same approach as described for Eq. (7). The discretization of Eqs. (9) and (10) is basically the same as Eqs. (7) and (8). The only difference is that the medium involved is that of Ω_1. The system equations can be expressed as

$$\sum_{n=1}^{N}\left(A^3_{mn}U^x_n + B^3_{mn}U^z_n + C^3_{mn}T^x_n + D^3_{mn}T^z_n\right) = b^3_m,$$
$$m = 1, 2, \ldots, N \quad , \tag{25}$$

and

$$\sum_{n=1}^{N}\left(A^4_{mn}U^x_n + B^4_{mn}U^z_n + C^4_{mn}T^x_n + D^4_{mn}T^z_n\right) = b^4_m,$$
$$m = 1, 2, \ldots, N \quad , \tag{26}$$

where $b^3_m = b^4_m = 0$ (for $m = 1, 2, \ldots, N$). Note that $A^3_{mm} = B^4_{mm} = -0.5$ and $B^3_{mm} = A^4_{mm} = 0$. Combining Eqs. (13), (20), (25), and (26), we have $4N$ linear algebraic equations with the same number of unknowns. The combined linear algebraic equations can be solved by direct methods such as Gauss-Jordan elimination or by iterative solvers such as conjugate gradient methods. In this paper, the conjugate gradient normalized residual method (CGNR) is used to solve the non-symmetric linear system (Barrett 1993). Next, we discuss how the fast multipole technique is used to formulate the same boundary element problem and solve it more efficiently.

4
Fast multipole technique

In the previous section, we discussed how the traditional BEM is used to solve the SIEs (1) and (2). We ended up with a large set of linear equation system which needs to be solved. As we said earlier, iterative methods are preferred over direct methods for large problems. For an iterative method, the most CPU intensive part is the matrix-vector multiplication. The number of floating-point operations (FPO) in a dense matrix-vector multiplication is of $O(N^2)$. The fast multipole method expedites this matrix-vector multiplication by a special treatment of interactions among widely separated segments. To use the technique, we divide the N segments of the scattering surface into groups based on the spatial distances. If we put M segments in each group, there are N/M groups altogether. Next, we discuss how the fast multipole method can be applied to our problem.

As we can see from the previous section, no matter how complicated they are, all matrix-element expressions are related to the Hankel functions, $H^{(1)}_0(k_p|\mathbf{r}_m - \mathbf{r}'|)$ and $H^{(1)}_0(k_s|\mathbf{r}_m - \mathbf{r}'|)$, and their derivatives in the integrands. If the two indices m, n of a matrix element belong to two separated groups, the integral for the matrix element can always be approximated by $H^{(1)}_0(k_p|\mathbf{r}_m - \mathbf{r}_n|)$, $H^{(1)}_0(k_s|\mathbf{r}_m - \mathbf{r}_n|)$, and their corresponding derivatives. Here, we assume that the group diameter is larger than one wavelength. Using the addition theorem, we have

$$H^{(1)}_0(kR_{mn}) = \sum_{p=-\infty}^{\infty} J_p(kd)H^{(1)}_p(kR_{ll'}) \times \mathrm{e}^{ip(\phi_d - \phi_{ll'} + \pi)} \quad , \tag{27}$$

where $\mathbf{R}_{mn} = \mathbf{r}_m - \mathbf{r}_n$, $\mathbf{R}_{ll'} = \mathbf{r}_l - \mathbf{r}_{l'}$, and $\mathbf{d} = \mathbf{R}_{ml} + \mathbf{R}_{l'n}\left(\mathbf{R}_{ml} = \mathbf{r}_m - \mathbf{r}_l,\ \mathbf{R}_{l'n} = \mathbf{r}'_l - \mathbf{r}_n\right)$. Here, $\phi_{ll'}$ is the angle the line $\mathbf{R}_{ll'}$ makes with the x axis, and we assume that the vector $\mathbf{d}$ makes an angle of ϕ_d with the x axis. Here, $\mathbf{r}_l$ and $\mathbf{r}_{l'}$ are the group centers. Substituting the elementary identity (Stratton 1941, Chew 1990),

$$J_p(kd)\mathrm{e}^{ip\phi_d} = \frac{1}{2\pi}\int_0^{2\pi} d\alpha \mathrm{e}^{i\mathbf{k}\cdot(\mathbf{R}_{ml}+\mathbf{R}_{l'n})+ip(\alpha-\pi/2)} \quad , \tag{28}$$

into Equation (27) yields

$$H_0^{(1)}(kR_{mn}) = \frac{1}{2\pi}\int_0^{2\pi} d\alpha \tilde{\beta}_{ml}(\alpha,k)\tilde{\alpha}_{ll'}(\alpha,k)\tilde{\beta}_{l'n}(\alpha,k) \quad , \tag{29}$$

where

$$\tilde{\alpha}_{ll'}(\alpha,k) = \sum_{p=-P}^{P} H_p^{(1)}(kR_{ll'})e^{ip(\alpha-\phi_{ll'}+\pi/2)} \quad , \tag{30}$$

and

$$\tilde{\beta}_{ml}(\alpha,k) = e^{i\mathbf{k}\cdot\mathbf{R}_{ml}}, \quad \tilde{\beta}_{l'n}(\alpha,k) = e^{i\mathbf{k}\cdot\mathbf{R}_{l'n}} \quad . \tag{31}$$

Notice that now, cylindrical waves are replaced by plane waves in the integrand of Eq. (29). Also, the $\tilde{\alpha}_{ll'}(\alpha)$ term is not dependent on a particular subscatterer but group centers, while $\tilde{\beta}_{ml}(\alpha)$ and $\tilde{\beta}_{l'n}$ depend on the transmitting and the receiving groups respectively. The series in Eq. (30) diverges if P increases indefinitely and appropriate truncation is needed in order to obtain the required accuracy. In fact, the divergence is due to the exchange of the order of the summation and the integration introduced in the derivation. The original addition theorem does not diverge because $J_p(kd) \to 0$, when $p \to \infty$. Given Eqs. (29)–(31), it is now trivial to express the derivatives in a similar fashion as following,

$$\frac{\partial^j H_0^{(1)}(kR_{mn})}{\partial x^j} = \frac{1}{2\pi}\int_0^{2\pi} d\alpha \tilde{\beta}_{ml}(\alpha,k)\tilde{\alpha}_{ll'} \times (\alpha,k)(ik\cos\alpha)^j \tilde{\beta}_{l'n}(\alpha,k) \quad , \tag{32}$$

and

$$\frac{\partial^j H_0^{(1)}(kR_{mn})}{\partial z^j} = \frac{1}{2\pi}\int_0^{2\pi} d\alpha \tilde{\beta}_{ml}(\alpha,k)\tilde{\alpha}_{ll'} \times (\alpha,k)(ik\sin\alpha)^j \tilde{\beta}_{l'n}(\alpha,k) \quad . \tag{33}$$

In order to show how FMM works, we take the mth row out of the submatrix $\mathbf{A}^1$ in Eq. (13) as an example and define

$$I_m = \sum_{n=1,N}^{n\notin B_l} A^1_{m,n} U^x_n \quad , \tag{34}$$

where m belongs to G_l, the lth group, and B_l represents the self group G_l and the near neighbor groups. Note that the submatrix $\mathbf{A}^1$ is used only to illustrate the FMM principle. In FMM, only the main diagonal and a few neighboring sub-diagonal elements need to be generated in the submatrix $\mathbf{A}^1$. Using Eqs. (29), (32), and (33), we have

$$\begin{aligned} I_m =& \frac{i}{8\pi}\int_0^{2\pi} d\alpha \tilde{\beta}_{ml}(\alpha,k_p) \sum_{l'=1,N/M}^{l'\notin B_l} \tilde{\alpha}_{ll'}(\alpha,k_p) \\ & \times \sum_{n\in G_{l'}} E(\alpha,k_p)\tilde{\beta}_{l'n}(\alpha,k_p)\Delta_n U^x_n \\ & + \frac{i}{8\pi}\int_0^{2\pi} d\alpha \tilde{\beta}_{ml}(\alpha,k_s) \times \sum_{l'=1,N/M}^{l'\notin B_l} \tilde{\alpha}_{ll'}(\alpha,k_s) \\ & \sum_{n\in G_{l'}} F(\alpha,k_s)\tilde{\beta}_{l'n}(\alpha,k_s)\Delta_n U^x_n \quad , \end{aligned} \tag{35}$$

where Δ_n is the size of the segment n. All the medium parameters are those of region Ω_0. For the interactions in the self group and the near neighbor groups, the matrix-vector multiplication is performed directly. The functions $E(\alpha,k_p)$ and $F(\alpha,k_s)$ are given as

$$\begin{aligned} E(\alpha,k_p) =& n'_x\left[\frac{\lambda}{2\mu+\lambda} ik_p\cos\alpha - \frac{2}{k_s^2}(ik_p\cos\alpha)^3\right] \\ & - n'_z\frac{2}{k_s^2}(ik_p\sin\alpha)(ik_p\cos\alpha)^2 \quad , \end{aligned} \tag{36}$$

and

$$\begin{aligned} F(\alpha,k_s) =& n'_x\left[\frac{2}{k_s^2}(ik_s\cos\alpha)^3 + 2ik_s\cos\alpha\right] \\ & + n'_z\left[\frac{2}{k_s^2}(ik_s\sin\alpha)(ik_s\cos\alpha)^2 + ik_s\sin\alpha\right] . \end{aligned} \tag{37}$$

The integrals in Eq. (35) can be simply evaluated with a staircase approximation. Thus, the equation can be re-written as

$$\begin{aligned} I_m =& \frac{i}{4Q}\sum_{q=1}^{Q} \tilde{\beta}_{ml}(\alpha_q,k_p) \sum_{l'=1,N/M}^{l'\notin B_l} \tilde{\alpha}_{ll'}(\alpha_q,k_p) \\ & \times \sum_{n\in G_{l'}} E(\alpha_q,k_p)\tilde{\beta}_{l'n}(\alpha_q,k_p)\Delta_n U^x_n \\ & + \frac{i}{4Q}\sum_{q=1}^{Q} \tilde{\beta}_{ml}(\alpha_q,k_s) \sum_{l'=1,N/M}^{l'\notin B_l} \tilde{\alpha}_{ll'}(\alpha_q,k_s) \\ & \times \sum_{n\in G_{l'}} F(\alpha_q,k_s)\tilde{\beta}_{l'n}(\alpha_q,k_s)\Delta_n U^x_n \quad , \end{aligned} \tag{38}$$

where Q is the number of discretization points for the integrals. It can be shown that Q has to be proportional to the group size in terms of wavelength from the sampling theorem. As we can see in Eq. (38), the interactions among the separated groups have been diagonalized by using plane wave bases, thus reducing the FPO count in the matrix-vector multiplication. In Eq. (38), the matrix-vector multiplication is performed in three stages by the three summation signs. Notice also that the operations have to be performed separately for compressional and shear waves. If we denote the three stages as 1, 2 and 3 starting from the last summation sign in Eq. (38), we see that the fields of the subscatterers in each group are translated to their group center in the first stage (group aggregation). Then, group interactions are calculated at the second stage (translation). Finally, these group interactions at each group are distributed to its group members (group disaggregation). Figure 2 demonstrates the major difference in the calculation of I_m between the FMM approach and the traditional dense matrix approach. As shown in Figs. 2(a) and 2(b), the calculation of I_m in a dense matrix approach involves direct interactions of the element m with all the other subscatterers, while FMM proceeds in a way as described above. In FMM, one needs to generate three sparse matrices instead of the dense matrix. These sparse matrices are associated with the three stages of the FMM matrix vector multiply procedure.

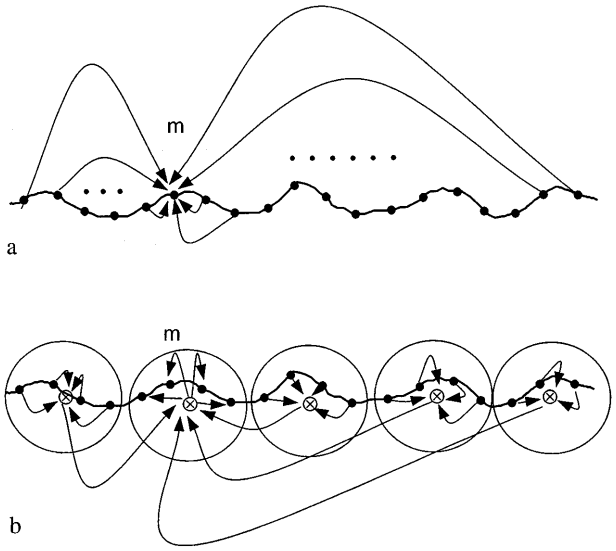

Fig. 2a, b. The major difference in the calculation of I_m between the traditional dense matrix approach (**a**) and the FMM approach (**b**)

The computational cost can be estimated in terms of the three stages outlined above in addition to the matrix-vector multiplication associated with the self group and the near neighbor groups. The FPO count is calculated as

$$T = c_1 \frac{N}{M} MQ + c_2 \left(\frac{N}{M}\right)^2 Q + c_3 M \frac{N}{M} Q + c_4 NM \quad , \tag{39}$$

where c_1, c_2, and c_3 are some constants associated with the three stages. The last term in the equation comes from the direct matrix-vector multiplication for the self group and the near neighbor groups. The coefficient c_4 is also a constant. Since Q is proportional to the group size M, the FPO count of the matrix-vector multiplication is proportional to $N^{1.5}$ if we choose $M = \sqrt{N}$. Actually, one should also notice that the speeds of the compressional and shear waves are different. Additional computational savings can be achieved if we choose different parameter Q for the different waves. For the two medium problem, usually four distinctive Q values can be used. Noticing that the largest Q corresponds to the fastest wave speed in the media, smaller Q's can be used for the other three speeds.

In the above discussion, the submatrix $\mathbf{A}^1$ is used to illustrate how matrix vector multiply is performed in the FMM approach. There are 16 similar submatrices in the whole problem as given by Eqs. (13), (20), (25), and (26). All the matrix vector multiplies has to be calculated similarly.

5
Ray-propagation fast multipole algorithm (RPFMA)

If one chooses the group size such that $M = N^{1/3}$, then Q is proportional to $N^{1/3}$. Eq. (39) can be rewritten as

$$T = c_1 N^{4/3} + c_2 N^{4/3} Q + c_3 N^{4/3} + c_4 N^{4/3} \quad . \tag{40}$$

In the above equation, all the terms have a FPO count proportional to $N^{4/3}$ except $c_2 N^{4/3} Q$ which corresponds to the group interactions. Thus, if we can reduce the cost of the group interactions, the computational complexity of the fast multipole method can be reduced. We now focus on the second stage of Eq. (38) which translates the fields radiated from a transmitting group in Q discretized directions into the same number of discretized directions at a receiving group. Intuitively, one expects the interaction to be strongest for fields radiated along the line joining the two groups. This is indeed the case, and forms the basis for the ray propagation technique (Wagner and Chew 1994; Coifman et al. 1994). In the ray propagation fast multipole algorithm, we neglect some of the interactions in side lobes which are much smaller than the main beam, thus reducing the cost of the second stage of FMM. As the problem size grows, the width of the main beam joining two groups decreases as $1/M$, while the number of angular sampling directions Q grows as M. Thus, the number of sampling directions in the main beam and the significant side lobes remains approximately constant as a function of problem size. Therefore, the remaining Q in Eq. (40) is independent of problem size if the small side-lobe interactions are ignored, and the ray propagation fast multipole algorithm has a computational complexity of $O(N^{4/3})$.

To take the full advantage of this idea, we use a tapered window function in the truncation of the summation terms in Eq. (30) instead of using a square window. The advantage of using a tapered window for Eq. (30) is that its Fourier transform will have lower side-lobes. These lower side-lobes will allow the discarding of more elements of $\alpha_{ll'}(\alpha, k)$ for a given threshold level and reduce the cost in the second stage of the fast multipole method.

6
Numerical results

A Fortran code has been developed based on the formulations of the fast multipole method to simulate various surface scattering problems. The results of the FMM code are shown to be as good as those of traditional dense-matrix BEM method and analytical method when available. As expected, the FMM code is much faster than the dense matrix approach and it requires much less memory. We have also parallelized the FMM code as well as the dense-matrix BEM code for the 4-processor SGI Power Challenge machine by using the MP commands. The FMM code scales very well when more CPUs are used. In what follows, we check the FMM code by comparing the FMM results with those of analytical method for a planar surface. Then, the FMM code is used to solve a rough surface scattering problem. The FMM results are compared with those of the dense-matrix BEM code for the rough surface case. Finally, the performance of the FMM code is checked against the dense-matrix BEM code in terms of the computer time usage and the memory requirement. The efficiency of parallelization for the FMM code is also addressed on the SGI Power Challenge computer ($4 \times$ R8000, 90 MHz, 2 GB RAM). We use BEM to represent the dense-matrix BEM method for simplicity. Notice that unless otherwise stated all the results given here are obtained on a four CPU SGI Power Challenge machine.

The FMM code is first verified for a two-layer elastic media with a planar interface. The incident wave $\mathbf{U}^{\text{inc}}$ used

is an asymptotic Gaussian beam modeled via the complex-source-point technique (Felsen 1984) and is given by,

$$\mathbf{U}^{\text{inc}} = \nabla\Phi^{\text{inc}}(k_p, R) \quad , \tag{41}$$

for compressional source, or

$$\mathbf{U}^{\text{inc}} = \nabla \times \left(\hat{\mathbf{y}}\Phi^{\text{inc}}(k_s, R)\right) \quad , \tag{42}$$

for shear wave source, where $R = [(x - x' - ib\sin\theta)^2 + (z - z' - ib\cos\theta)^2]^{1/2}$ and $\text{Re}\{R\} > 0$. Here, b is a constant which determines the width of the beam source, and θ is the incident angle of the beam axis, measured with respect to the z axis. The Gaussian beam $1/e$ width w is related to b by $b_{p,s} = 0.5w^2k_{p,s}$. The potential function in Eq. (41) and (42) is defined as

$$\Phi^{\text{inc}}(k, R) = \frac{1}{\sqrt{8\pi kR}} e^{ikR + i\frac{\pi}{4} - kb} \quad , \tag{43}$$

which is the large argument approximation of the zeroth order Hankel function of the first kind.

The parameters of the two elastic media are given as $\rho_0 = 1,400\,\text{kg/m}^3$, $c_{p0} = 3,000$ m/s, $c_{s0} = 2,000$ m/s, $\rho_1 = 2,700\,\text{kg/m}^3$, $c_{p1} = 6,400$ m/s, and $c_{s1} = 3,700$ m/s. The compressional source is used and is located at $x = 0$, $z = -4.17\,\lambda_{p0}$, where λ_{p0} is the wavelength of the compressional waves in Ω_0. The parameter w of the asymptotic beam source is chosen to be $2.56\,\lambda_{p0}$. Based on our formulation, the scattered fields can be simulated by FMM. For a well-welded planar interface, the reflected fields and the transmitted fields can also be calculated analytically by the real axis integration (RAI) in the wave number domain (see Appendix).

Figures 3–4 show the comparison of scattered fields calculated by FMM with those calculated by the RAI approach. The curves shown in the figures are the x and z components of the displacement fields at different locations. The medium interface is at $z = 0$. The vertical location (z) of the observation line is denoted in each figure. Both the vertical location and the horizontal axis are in the unit of wavelength λ_{p0}. A compressional source is used here. The source is located at $x = 0$, $z = -4.17\,\lambda_{p0}$ with $\omega = 2.56\,\lambda_{p0}$. In Fig. 3, we have a compressional beam source insonifying on the surface with an incident angle of 20°. While the lines of observation are always parallel to the medium interface for all the figures, the observation position of the z coordinate determines whether the calculated fields are the fields of reflections or transmissions. If $z < 0$, the curves represent the reflected fields. Otherwise, the transmitted fields are plotted. These descriptions hold true also for Fig. 4 except that the incident angle of the source is at 50° and $w = 3.33\,\lambda_{p0}$, where λ_{p0} is the wavelength of the compressional waves in Ω_0. As we can see from the figures, excellent agreement is achieved for all the cases between the FMM and RAI results. Since the source is not well-collimated, it excites surface waves even when the incident angle of the beam axis is at 20° as shown

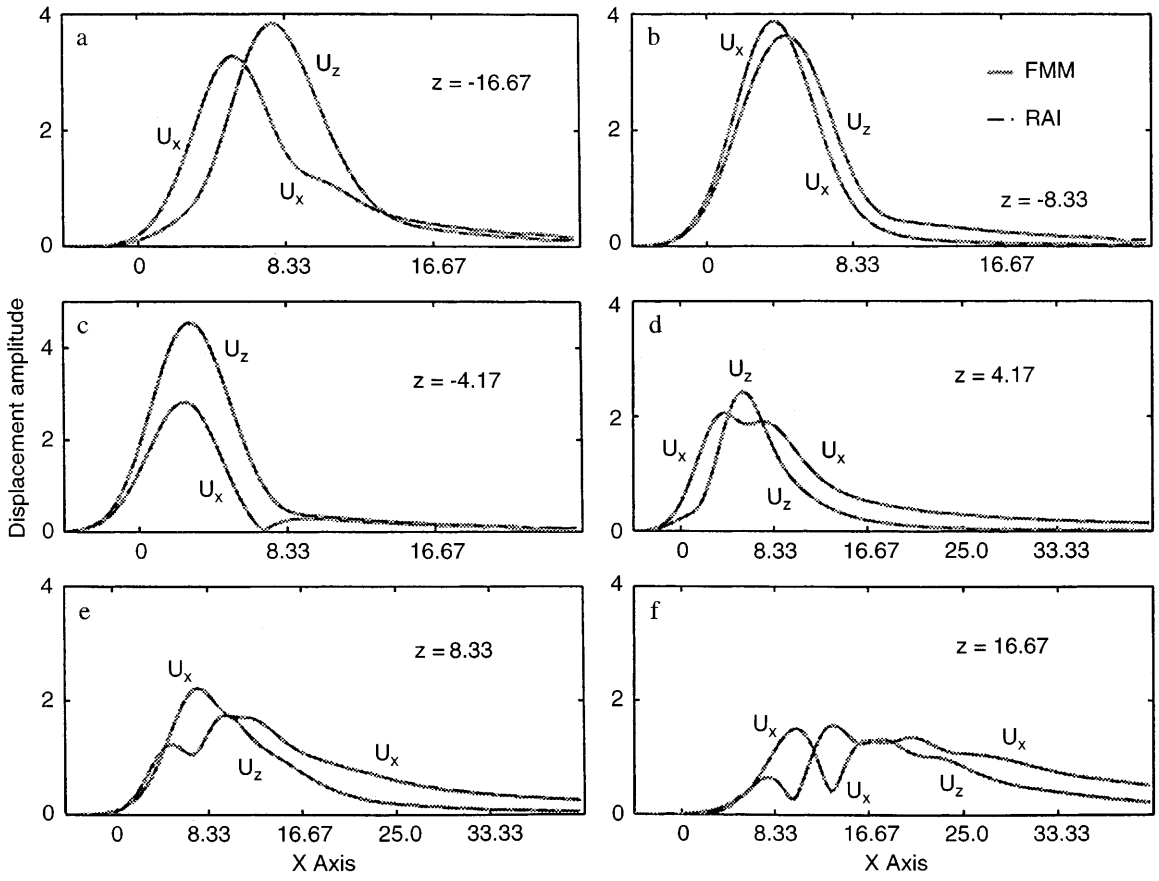

Fig. 3. Comparison of the scattered fields of a planar surface simulated by FMM and the real axis integration (RAI) in the wave number domain

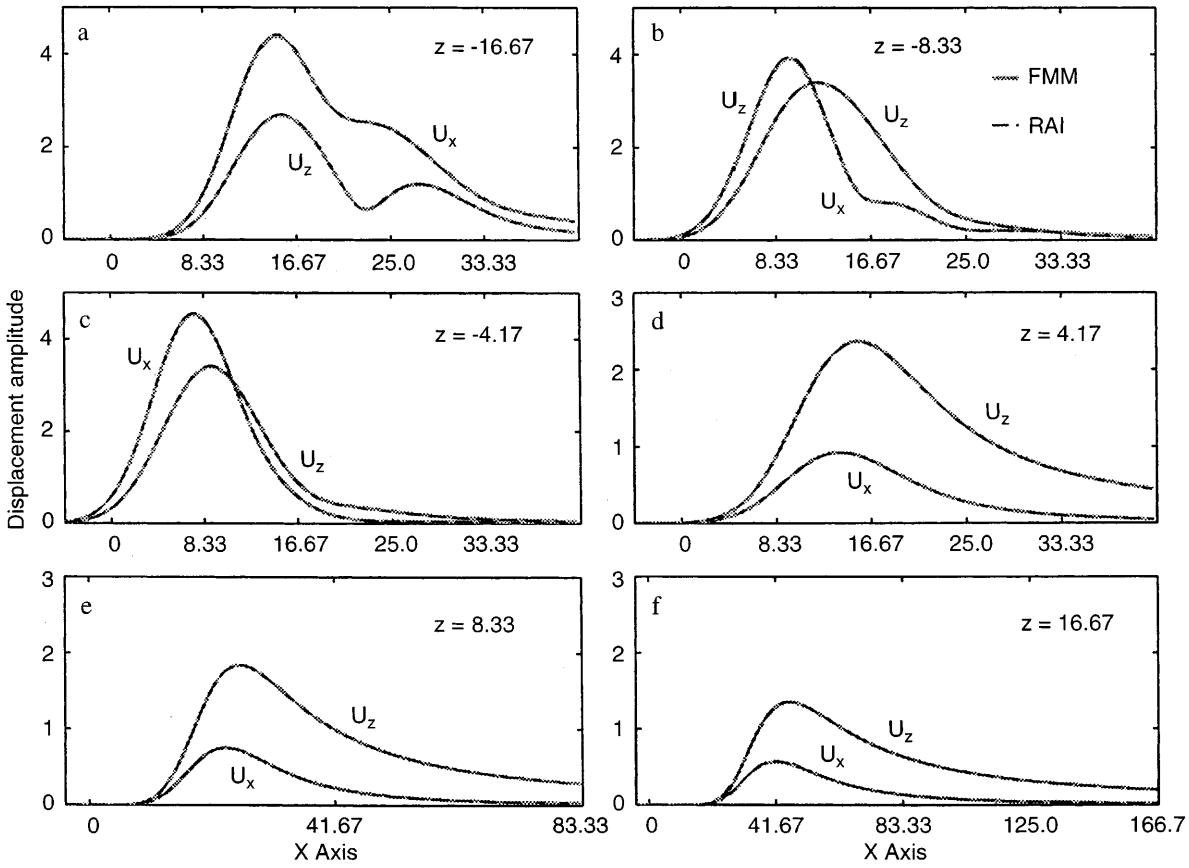

Fig. 4. Same as Fig. 3

in Fig. 3. The surface waves become stronger as the incident angle increases from 20° to 50°. Due to the existence of the surface waves, we have to solve a much larger surface area, especially when the incident angle is high. In Fig. 4, a surface of roughly 90 wavelengthes is discretized into 1,340 segments (15 points per wavelength). A linear equation set of 5,360 unknowns is solved using FMM.

Figure 5 is a rough surface scattering problem encountered in geophysical well logging. The x axis and the height of the rough surface are in the unit of wavelength λ_{p0}. The overlaid curves are the incident displacement fields at the rough surface. The amplitude of the incident fields is reduced by a factor of 10 for display. The medium parameters are the same as those used for the planar interface given in Fig. 3. Again, the asymptotic Gaussian beam source is used. We put the source at $x = 0$, $z = -4.17\,\lambda_{p0}$ with an incident angle of 30°, $w = 2.56\,\lambda_{p0}$. Both the FMM and the dense-matrix BEM codes are used to calculate the reflected fields by the rough surface. The simulated results are shown in Figs. 6 and 7, where the reflected displacement fields from the FMM code are overlaid with those of the BEM code. The field amplitude is given in the unit of wavelength λ_{p0}. The observation line is at $z = -4.17\,\lambda_{p0}$ for Fig. 6 and at $z = -8.33\,\lambda_{p0}$ for Fig. 7. As we can see from the figures, FMM does not cause any noticeable error in the simulation. However, the computational saving is drastic. For this particular problem, the rough surface is discretized into 1,740 segments. The number of unknowns solved is 6,960. For a convergence residual of 5.0×10^{-6}, the CPU time used for FMM is only 7 minutes, or less than one fifth of the CPU time needed for the BEM method.

Figure 8 shows the CPU time needed in each CG iteration for FMM as compared with the traditional BEM. The $N^{1.5}$ and N^2 lines are also plotted for references. FMM is shown to have a computational complexity better than

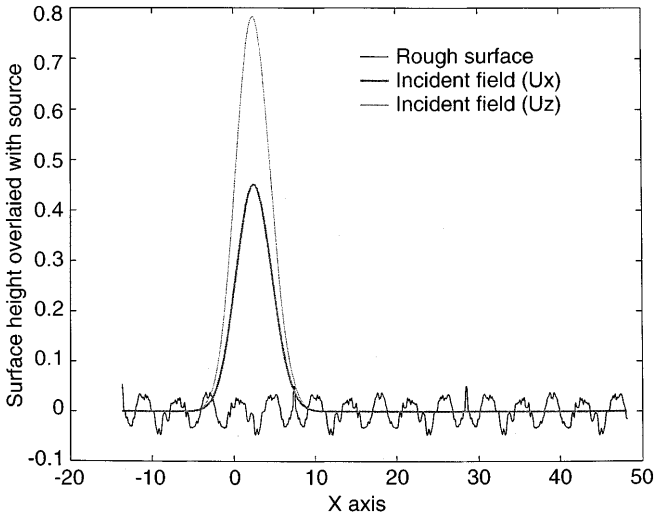

Fig. 5. A rough surface model used for simulation by using FMM and BEM

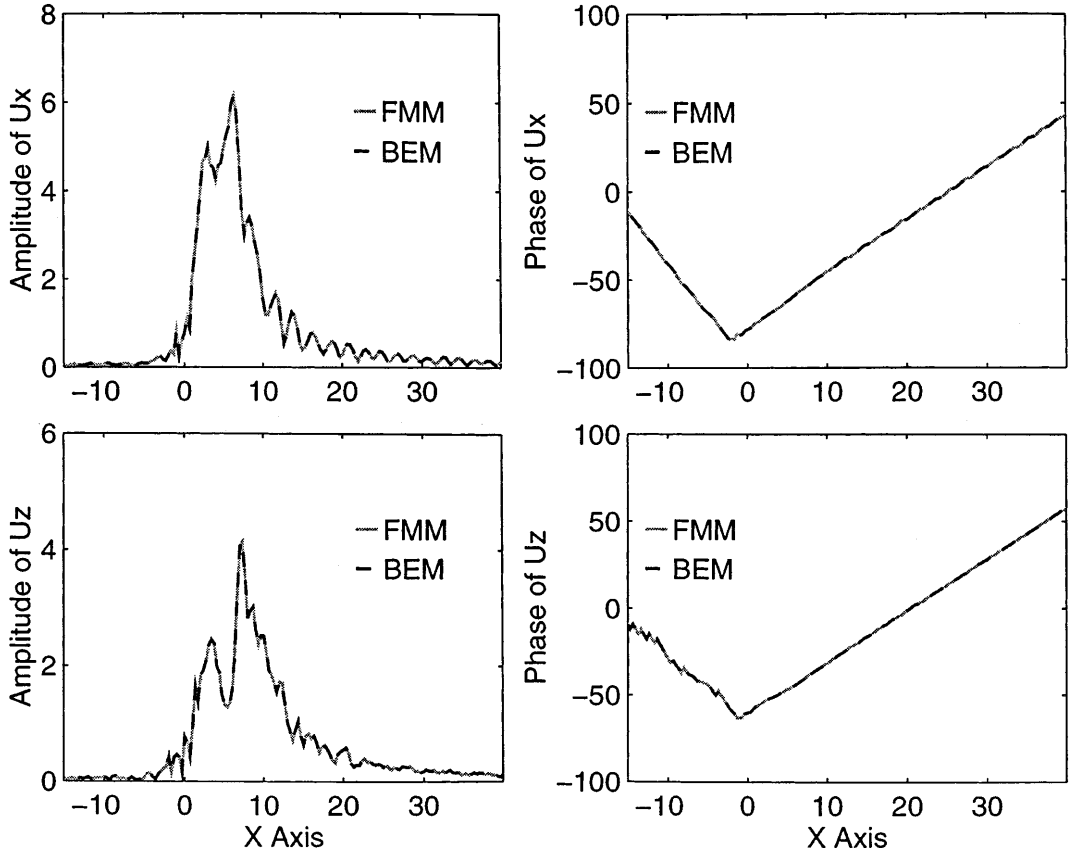

Fig. 6. Comparison of the reflected fields from a rough surface simulated by FMM and BEM

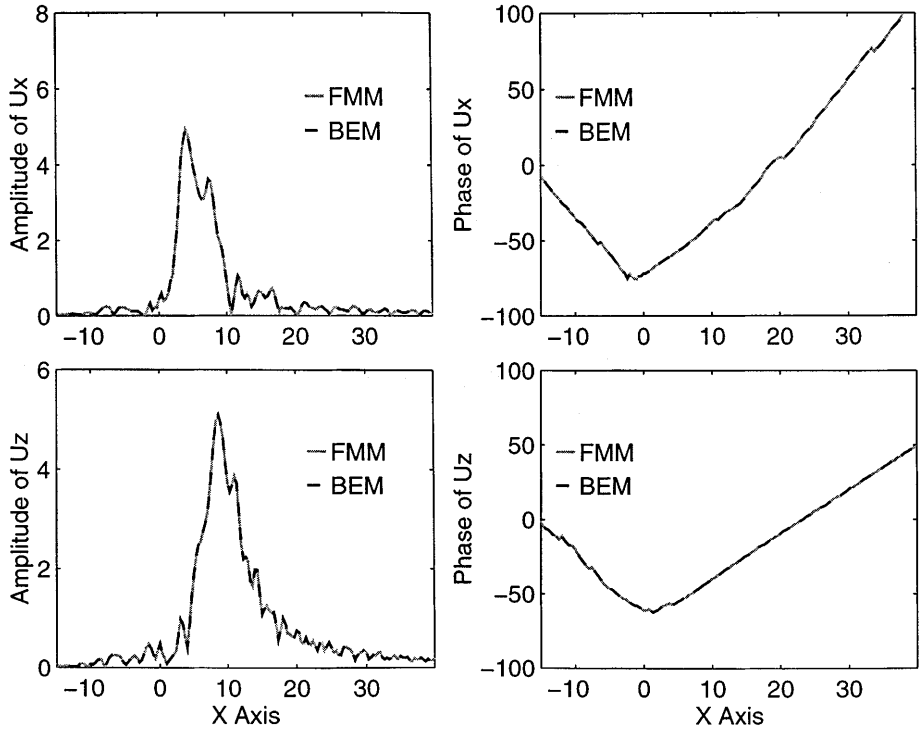

Fig. 7. Same as Fig. 6

$O(N^{1.5})$. BEM, however, shows a complexity along the N^2 line. The computer used here is an SGI Power Challenge with four CPUs. While the CPU time might be affected by various factors such as the problem size, the system load at the time, the parallelization effects, and etc. When the problem size is small, the parallelization is usually not very efficient. When the problem size is large, one major problem of the SGI computer is cache misses. In BEM, one

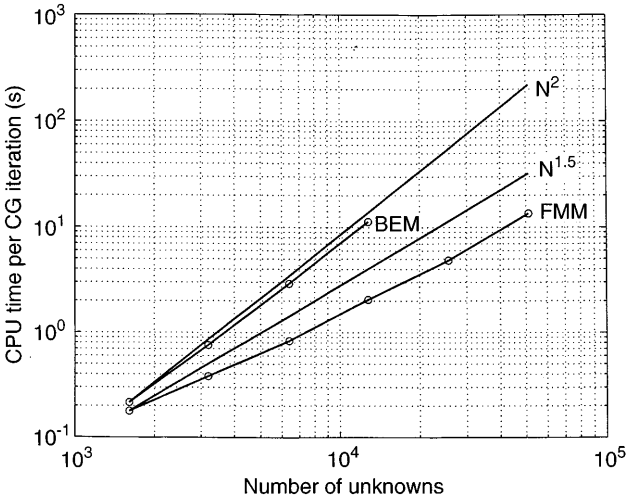

Fig. 8. Comparison of the CPU time needed in each CG iteration for traditional BEM and FMM

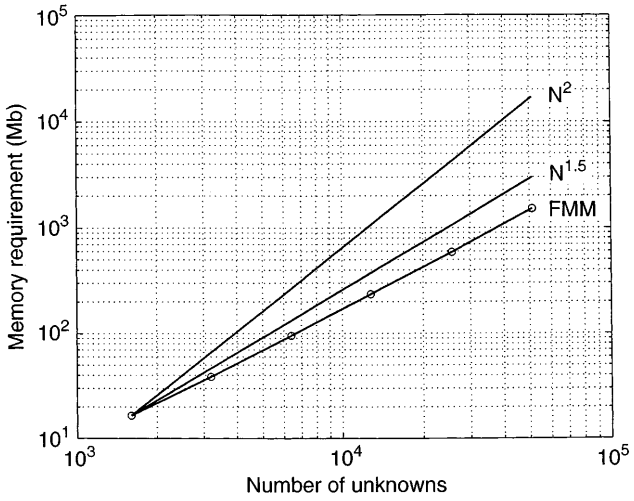

Fig. 10. The memory requirement of FMM as compared with dense matrix methods

needs to do $\mathbf{A}^{\dagger} \cdot \mathbf{x}$ as well as $\mathbf{A} \cdot \mathbf{x}$. Because of the way in which system memory is accessed, the latter will cost much more than the former if the cache miss problem is not properly addressed. For FMM, the dense matrix is decomposed into a set of sparse matrices, and this problem is not very obvious. The comparison of the matrix filling time for the two methods is given in Fig. 9. The same trend is observed again. The difference is that the BEM line now is below the N^2 line, because the matrix filling process does not need to access the dense matrix line by line in the horizontal direction. FMM is also much better than BEM when the memory requirement is considered. As shown in Fig. 10, the memory requirement of FMM is also below the $N^{1.5}$ line. Notice that the problem solved here is the two medium model with a planar interface as given earlier. Different size problems are obtained by simply increasing the surface size to be discretized. The largest problem solved by BEM has 12,800 unknowns and the solve time is more than 1.5 hours on the four-CPU SGI computer for a convergence residual of 5.0×10^{-6}. By using FMM, only 16 minutes is required to solve the same problem. The largest problem solved here by FMM has 51,200 unknowns. The CPU time needed to solve such a large problem is less than 3 hours. It is estimated that more than 40 hours is required if the traditional BEM is used on the SGI computer. The memory requirement for the dense matrix is approximately 20 GB. Figure 11 demonstrates the efficiency of our FMM code when more than one CPU is used. 10,000 unknowns are used for the test. As we can see from the figure, the matrix filling parallelizes better than the CG solver part. The former achieves almost linear speedup. A factor of 3.2 speedup is achieved for the CG solver when four CPUs are used.

7 Conclusions

The fast multipole method is applied to the simulation of surface scattering problems for elastic waves, which has not been done before to our knowledge. An efficient code is developed to solve the surface integral equations for a

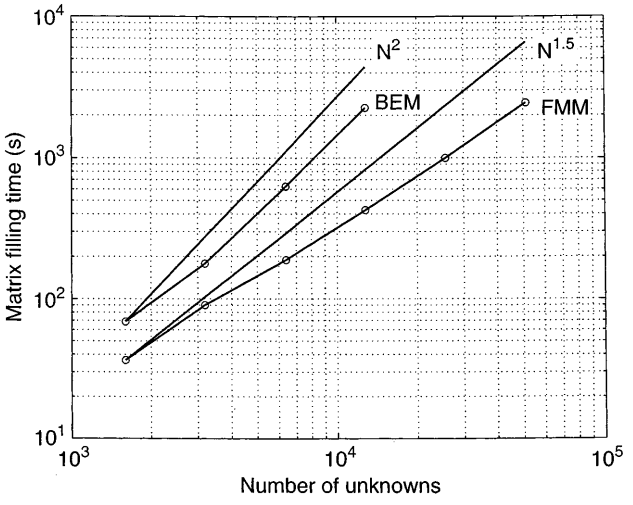

Fig. 9. The matrix filling time comparison of BEM and FMM

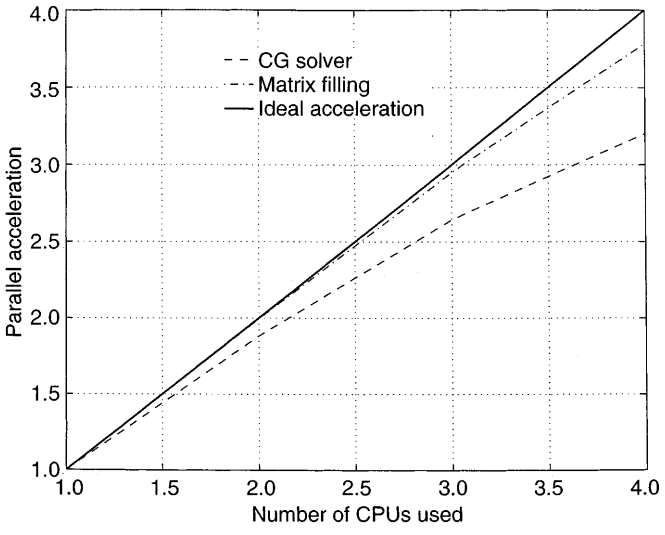

Fig. 11. Speedup of multi-CPU simulation by using FMM

solid-solid interface. In terms of computational complexity, the code is better than $O(N^{1.5})$ in both the CPU time and the memory requirement. The code is first verified by the analytical results for a planar interface model, and then tested by a dense-matrix BEM approach for a prototype rough surface. Our results show that FMM, as a rigorous method, is not only fast, but also very accurate. We have also parallelized the code for the SGI Power Challenge machine. Approximately linear speedup is achieved for the matrix filling. A factor of 3.2 is achieved for the CG solver when 4 CPUs are used.

Appendix A

Beam reflection and transmission at a planar solid-solid interface

In this appendix, we present the wavenumber integral representation we used for the problem of reflection and transmission of a Gaussian beam at a planar solid-solid interface. These integral solutions are numerically implemented using a real axis integration scheme. They are used to generate reference data for the FFM numerical solutions for the canonical case of a planar interface. The geometry of the 2D configuration considered is shown in Fig. 1 with the addition that a 2D (sheet) Gaussian beam input is assumed to insonify in the $+z$ direction a planar interface at $z = 0$ separating medium 0 $(v_{p_0}, v_{s_0}, \rho_0)$ from medium 1 $(v_{p_1}, v_{s_1}, \rho_1)$. The Gaussian beam is modeled via the complex-source-point (CSP) technique by displacement of a real point source into complex space as specified by Eqs. A.7 below (Felson 1984). Using a plane wave expansion of the incident elastic CSP wavefield, the reflected $(\mathbf{U}^{\mathrm{ref}})$ and transmitted $(\mathbf{U}^{\mathrm{tr}})$ displacement fields at an observation point (x, z) can be derived from compressional $(\Phi^{\mathrm{ref,tr}})$ and shear $(\Psi^{\mathrm{ref,tr}})$ scalar potentials as follows (Zeroug and Stanke 1996),

$$\mathbf{U}^{\mathrm{ref,tr}} = \nabla\Phi^{\mathrm{ref,tr}} + \nabla \times \left(\mathbf{y}\Psi^{\mathrm{ref,tr}}\right) \ , \tag{A.1}$$

where

$$\begin{Bmatrix} \Phi^{\mathrm{ref}}(x,z) \\ \Psi^{\mathrm{ref}}(x,z) \end{Bmatrix} = \frac{i}{4\pi}\int_{-\infty}^{\infty} \frac{1}{\kappa_{v0}} \begin{Bmatrix} R_{vp}(k)\exp\left[i\mathscr{P}_{\Phi}^{\mathrm{ref}}(k)\right] \\ R_{vs}(k)\exp\left[i\mathscr{P}_{\Psi}^{\mathrm{ref}}(k)\right] \end{Bmatrix} \mathrm{d}k \ , \tag{A.2}$$

$$\begin{Bmatrix} \Phi^{\mathrm{tr}}(x,z) \\ \Psi^{\mathrm{tr}}(x,z) \end{Bmatrix} = \frac{i}{4\pi}\int_{-\infty}^{\infty} \frac{1}{\kappa_{v0}} \begin{Bmatrix} T_{vp}(k)\exp\left[i\mathscr{P}_{\Phi}^{\mathrm{tr}}(k)\right] \\ T_{vs}(k)\exp\left[i\mathscr{P}_{\Psi}^{\mathrm{tr}}(k)\right] \end{Bmatrix} \mathrm{d}k \ , \tag{A.3}$$

with

$$\begin{Bmatrix} \mathscr{P}_{\Phi}^{\mathrm{ref}}(k) \\ \mathscr{P}_{\Phi}^{\mathrm{ref}}(k) \end{Bmatrix} = k(x-\tilde{x}') - \kappa_{v_0}\tilde{z}' - \begin{Bmatrix} \kappa_{p_0} \\ \kappa_{s_0} \end{Bmatrix} z \ , \tag{A.4}$$

$$\begin{Bmatrix} \mathscr{P}_{\Phi}^{\mathrm{tr}}(k) \\ \mathscr{P}_{\Phi}^{\mathrm{tr}}(k) \end{Bmatrix} = k(x-\tilde{x}') - \kappa_{v_0}\tilde{z}' + \begin{Bmatrix} \kappa_{p_1} \\ \kappa_{s_1} \end{Bmatrix} z \ . \tag{A.5}$$

In the equations above, $v \equiv p$ for an incident compressional beam and $v \equiv s$ for an incident shear beam, R_{vp}, R_{vs}, T_{vp} and T_{vs} are the spectral plane wave reflection (R) and transmission (T) coefficients for a well-welded solid-solid interface. The expressions for these quantities are given by Zeroug and Stanke (1996). Furthermore,

$$\kappa_{v_i} = \sqrt{k_{v_i}^2 - k^2}, \quad \mathrm{Re}\{\kappa_{v_i}\} \geq 0, \quad \mathrm{Im}\{\kappa_{v_i}\} \geq 0; \quad k_{v_i} = \omega/v_{v_i} \ , \tag{A.6}$$

where $v \equiv p, s$. The CSP coordinates $(\tilde{x}', \tilde{z}')$ are given by,

$$\tilde{x}' = x' + ib\sin\theta, \quad \tilde{z}' = z' + ib\cos\theta, \tag{A.7}$$

where (x', z') denote the location of the Gaussian beam waist and the CSP parameter b is related to the beam $1/e$ width w through $w = \sqrt{2b/k_{v_0}}$. The beam axis makes an angle θ with respect to the z axis.

References

Barrett R, Berry M, Chan TF, Demmel J, Donato J, Dongarra J, Eijkhout V, Pozo R, Romine C, Vorst H (1993) Templates for the Solution of Linear Systems. Building Blocks for Iterative Methods: SIAM Publication, 14–18

Brebbia CA, Telles JCF, Wrobel LC (1984) Boundary Element Techniques. Springer-Verlag, 177–236

Chew WC (1990) Waves and fields in inhomogeneous media. Van Nostrand Reinhold, 62–63

Coifman R, Rokhlin V, Wandzura S (1993) The fast multipole method for the wave equation: A pedestrian prescription. IEEE Antennas Propagat. Mag., 35, 7–12

Coifman R, Rokhlin V, Wandzura S (1994) Faster single-stage multipole method for the wave equation. 10th Annual Review of Progress in Applied computational Electromagnetics, 19–24

Cole DM, Kosloff DD, Minister JB (1978) A numerical Boundary Integral Equation Method for Elastodynamics. I. Bull Seismol. Soc. Am. 28, 288–291

Engheta N, Murphy WD, Rokhlin V, Vassiliou MS (1992) The fast multipole method (FMM) for electromagnetic scattering problems. IEEE Trans. Antennas Propagat. AP-40, 634–641

Felsen LB (1984) Geometrical theory of diffraction, evanescent waves, complex rays and Gaussian beams. Geophys. J. Royal Astro. Soc. 79, 77–88

Harrington RF (1968) Field Computation by Moment Methods. Krieger Publishing Company

Lu CC, Chew WC (1993) A fast algorithm for solving hybrid integral equation. IEE Proc. Pt. H 140 455–460

Manolis GD, Beskos DE (1988) Boundary Element Methods in Elastody-namics. Unwin Hyman Ltd

Morse PM, Feshbach H (1953) Methods of theoretical physics. McGraw-Hill, New York

Nihei KT, Myer LR, Cook NGW (1995) Numerical simulation of elastic wave propagation in granular rock with the boundary integral equation method. J. Acoust. Soc. Am. 97, 1423–1434

Pao YH, Varatharajulu V (1976) Huygens' principle, radiation conditions, and integral formulas for the scattering of elastic waves. J. Acoust. Soc. Am. 59, 1361–1371

Rizzo FJ (1967) An integral equation approach to boundary value problems of classical elastostatics. Q. Appl. Math. 25, 83–95

Rokhlin V (1990) Rapid solution of integral equations of scattering theory in two dimensions: J Comput. Phys. 86, 414–539

Song J, Chew WC (1994) Fast multipole method solution using parametric geometry. Microwave and Opt. Tech. Lett. 7, 60–765

Stratton JA (1941) Electromagnetic Theory. McGraw-Hill, New York

Tsang L, Kong JA, Shin RT (1985) Theory of microwave remote sensing. John Wiley Sons, Inc.
Varadan VV, Lakhtakia A, Varadan VK (1991) Field representation and introduction to scattering. North-Holland (Chap. 2, Sect. 7)
Wagner R, Chew WC (1995) A study of wavelets for the solution of electromagnetic integral equations: IEEE Trans. Antennas Propagat AP-43, 802–810
Wagner RL, Chew WC (1994) A ray-propagation fast multipole algorithm. Microwave Opt. Technol. Lett. 7, 435–438
Zeroug S, Stanke FE (1996) Ultrasonic pulsed beam interaction with a fluid-loaded elastic plate: theory. J. Acoust. Soc. Am. 100 1339–1348
Zeroug S, Stanke FE (1996) Ultrasonic pulsed beam interaction with a fluid-loaded elastic plate: Experimental validation. J Acoust. Soc. Am. 100 1349–1356